PONTIFICIA UNIVERSIDAD CATOLICA DE CHILE
SCHOOL OF ENGINEERING

ANALYSIS, DESIGN AND TESTING OF AN HOURGLASS-SHAPED ETP-COPPER ENERGY DISSIPATION DEVICE

BENJAMÍN ANDRÉS BRIONES GRANDI

Thesis submitted to the Office of Research and Graduate Studies
in partial fulfillment of the requirements for the degree of
Master of Science in Engineering

Advisor:
JUAN CARLOS DE LA LLERA MARTÍN

Santiago de Chile, July 2013

PONTIFICIA UNIVERSIDAD CATOLICA DE CHILE
SCHOOL OF ENGINEERING

ANALYSIS, DESIGN AND TESTING OF AN HOURGLASS-SHAPED ETP-COPPER ENERGY DISSIPATION DEVICE

BENJAMÍN ANDRÉS BRIONES GRANDI

Members of the Committee:
JUAN CARLOS DE LA LLERA MARTÍN
ESTEBAN SÁEZ ROBERT
ANDRÉ COTÉ
IGNACIO LIRA CANGUILHEM

Thesis submitted to the Office of Research and Graduate Studies
in partial fulfillment of the requirements for the degree of
Master of Science in Engineering

Santiago de Chile, July 2013

Gratefully to my family

TABLE OF CONTENTS

LIST OF FIGURES

LIST OF TABLES

ABSTRACT

The behavior of a bi-directional metallic energy dissipation device made of ETP-copper (Cu-BEDD) is presented. The development considered four phases: (1) Characterization and numerical modeling of the cyclic plastic behavior of ETP copper using the Chaboche constitutive model; (2) Generation of a FE model including large deformations and the inelastic constitutive model of the material; (3) Numerical design of the Cu-BEDD using design of experiments theory; and (4) Testing of two different proof-of-concept devices obtained from design in both, a one-directional displacement loading, and a bi-directional loading path. The cyclic response of the device showed great energy dissipation capacity even from very small deformations. It was also capable of enduring more than 20 cycles, corresponding to more than one strong earthquake, prior to failure. Also, the numerical model was capable of representing the cyclic response characteristics of the Cu-BEDD very accurately, and the proposed design process was validated using the measured response of the tested devices. It is concluded that the design procedure developed proved to be a very cost-effective and versatile method that can be applied to the design of other metallic dampers.

Keywords: damper; copper; energy dissipation; plasticity

RESUMEN

Se ha desarrollado con éxito un disipador de energía metálico construido de cobre ETP, que funciona en dos direcciones de desplazamiento (Cu-BEDD). El desarrollo fue llevado a cabo en cuatro etapas: (1) Caracterización y representación numérica del comportamiento cíclico del cobre ETP con incrusión en el rango plástico, utilizando el modelo constitutivo de Chaboche; (2) Generación de un modelo de elementos finitos incluyendo grandes deformaciones y el modelo constitutivo del cobre; (3) Diseño del Cu-BEDD utilizando la teoría de diseño de experimentos aplicada a experimentos numéricos; (4) Ensayo de prototipos tanto en una como en dos direcciónes de desplazamiento relativo. La respuesta cíclica de los Cu-BEDD ensayados muestra una gran capacidad para disipar energía al ser sometido a un desplazamiento relativo cíclico, incluso a amplitudes pequeñas, resistiendo además una cantidad de ciclos a grán amplitud equivalente a más de dos sismos severos. La respuesta numérica obtenida del modelo de elementos finitos muestra una correcta representación de la mayoría de las características de los resultados obtenidos de los ensayos de los prototipos. Adicionalmente, el proceso de diseño fue validado utilizando la respuesta experimental de los Cu-BEDD, demostrando ser un método versátil y de bajo costo, el cual puede ser utilizado en el diseño de otros disipadores de energía metálicos.

Palabras Claves: disipador de energía, disipador metálico, cobre, plasticidad

1. INTRODUCTION

Passive energy dissipation devices, such as viscous dampers, viscoplastic dampers, friction dampers, and metallic dampers, have been widely developed, implemented and validated as seismic protection systems in the last twenty years (Shen & Soong, 1996; Soong & Spencer Jr, 2002; Symans et al., 2008). In particular, metallic dampers are among the most commonly used due to their simplicity and low cost. Figures obtained from a number of local projects (SIRVE S.A., 2003) show that, metallic dampers cost about 0.07 dollars per joules. This figure may be contrasted with about 0.13 dollars per joule for viscous dampers, hence, if maintenance costs are neglected, viscous dampers essentially double the cost of metallic dampers, but require no eventual replacement after a large earthquake.

In the case of metallic dampers, the energy is dissipated by cyclic yielding of the base metal. Various devices using different mechanisms to produce yielding have been presented in the literature. These include the shear panel (Nakashima et al., 1994; De Matteis, Landolfo, & Mazzolani, 2003), in which a shear force induces in-plane yielding of a metallic plate; the well-known ADAS (Whittaker, Bertero, Thompson, & Alonso, 1991; Xia & Hanson, 1992; Tehranizadeh, 2001) and TADAS (Tsai, Chen, Hong, & Su, 1993; Chou & Tsai, 2002), which work based on out-of-plane bending and yielding; the honeycomb (Kobori et al., 1992) and the slit dampers (Chan & Albermani, 2008), which undergo in-plane bending and shear simultaneously; the buckling restrained brace (BRB) (Kim & Choi, 2004; Black, Makris, & Aiken, 2004; Miller, Fahnestock, & Eatherton, 2011; López-Almansa, Castro-Medina, & Oller, 2012), composed of a metallic core that yields in both, tension and compression, and is constrained by a steel casing filled with mortar or concrete to prevent buckling in compression; and a thin wall cylindrical tube, conceived to work exclusively in torsion (Franco, Cahís, Gracia, & López, 2010).

Bi-directional metallic dampers have also been developed and implemented (Kobori, Yamada, Takenaka, Maeda, & Nishimura, 1988; Kobori et al., 1992; Castellano, Colato, & Infanti, 2009); they absorb energy from the 2D-relative displacement of two points in parallel planes within a structure. Examples of 2D-metallic dampers are the bell-shaped dampers tested and installed as connectors between two adjacent buildings (Kobori et al., 1988), and the hourglass-shaped bi-directional damper installed in the expansion joints between steel frame sections of an indoor sky slope structure (Kobori et al., 1992). Additionally, an isolation system, which comprises sliders with a set of bi-directional energy dissipation devices was implemented in the Marquam Bridge, Oregon, USA (Martelli, 2008), and in the Tuy Medio Railway Viaducts located in Venezuela (Chiarotto, Tomaselli, Baldo, Castellano, & Infanti, 2004). Bi-directional metallic dampers have proved to reduce effectively the earthquake responses of a wide range of structures (Martelli, 2008; Castellano et al., 2009).

Energy dissipation devices made of carbon steel have proved to be very effective in reducing the earthquake response of structures; the use of alternatives to steel, such as shape memory alloys (McCormick & DesRoches, 2004; Song, Ma, & Li, 2006), lead (Casciati, Faravelli, & Petrini, 1998; Rodgers, Denmead, Leach, & Chase, 2006; Rodgers et al., 2008), and aluminum (De Matteis, Mazzolani, & Panico, 2008; Sahoo & Rai, 2010; Rai, Annam, & Pradhan, 2013; Wang, Usami, Funayama, & Imase, 2013) have also been thoroughly investigated. In the past an annealed copper ADAS damper was developed and tested showing an excellent cyclic behavior and large energy dissipation capacity (De la Llera, Esguerra, & Almazán, 2004; Moroni, Herrera, & Sarrazin, 2008). In addition to some mechanical advantages in terms of high plasticity and low-cycle fatigue life (Stephens, Fatemi, Stephens, & Fuchs, 2001; Li, Zhang, Sun, & Li, 2011; Zhang & Jiang, 2006), high-purity copper has an outstanding resistance to corrosion, it can be easily smelted and reused once it has already been damaged due to plastic deformation, and has considerable aesthetic advantages relative to other metals. Shown in Figure 1.1 is the relative cost of copper to steel in the last twelve years. Carbon steel has become a very competitive material for energy dissipation devices due to its extremely low relative cost (ratio about 1:10), which indicates that copper energy dissipation devices must be designed not only to maximize the energy dissipated during an earthquake, but also to minimize its weight in order to be commercially competitive.

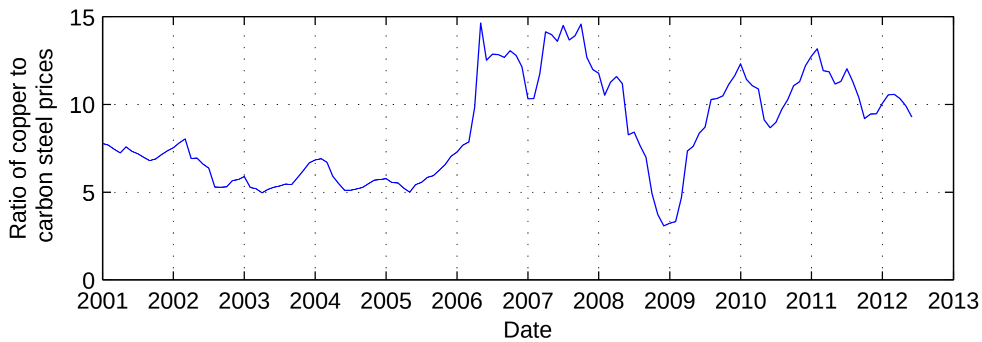

FIGURE 1.1. Historical prices of copper and hot rolled carbon steel.

The combination of two ideas, an exploration of copper-based energy dissipation devices and bi-directional behavior, motivated the current research. This research on the development of a copper-based Bi-directional Energy Dissipation Device (Cu-BEDD) includes a finite element (FE) model that incorporates large displacements, and an inelastic plasticity constitutive model previously proposed by Chaboche (Chaboche, 1986), which considers kinematic and isotropic hardening together with memory effect. This model has been used extensively for mechanical applications, such as spring back prediction (Broggiato, Campana, & Cortese, 2008; Lee et al., 2005; Zang, Guo, Thuillier, & Lee, 2011) and the cyclic response of structural steels with a yield plateau (Ucak & Tsopelas, 2011). The constitutive model parameters were calibrated for electrolitic tough pitch (ETP) copper using cyclic uniaxial tests. Once the constitutive model parameters were calibrated, the FE model was used to optimize the geometry of the Cu-BEDD, such that it maximizes the energy dissipated for a given displacement cycle, using the response surface methodology (Pukelsheim, 2006) . As far as the authors know the use of this constitutive model to predict the behavior of a copper energy dissipation device is novel. Also, the devices were tested in order to evaluate the true behavior of the designed Cu-BEDD, validate their design process, and evaluate the prediction capability of the FE model used. The Cu-BEDD probes were tested under cyclic displacement of constant amplitude and multistep tests with increasing displacement amplitudes until reaching failure. Two different designs for the device were tested, which were obtained from the geometry optimization process, and an additional device was tested bi-directionally in two perpendicular directions until failure. The response measured was compared with the one obtained numerically, and valuable information is derived for future product development.

2. MECHANICAL PROPERTIES

Mechanical properties of pure copper make it a very competitive material for energy dissipation due to its highly plastic behavior, specially when annealed. In particular, this investigation uses Electrolytic Tough Pitch (ETP) Copper, defined by a minimum copper concentration of 99.9%, perhaps one of the most common commercially available coppers. The linear elastic properties of ETP copper are $E = 115$ GPa, $G = 43$ GPa, and $\nu = 0.33$ (*ASM Metals Handbook, Vol. 2*, 2004). The tensile strength is about $\sigma_t = 233$ MPa, and the yield stress $\sigma_y = 40$ MPa. Its maximum elongation is $\varepsilon_u = 50$ %, and its density $\gamma_{Cu} = 8.89\ g/cm^3$ at $20°C$ (*ASM Metals Handbook, Vol. 2*, 2004).

When copper is subjected to cyclic strain, as it is for the case of metallic dampers, several material properties can be measured. Standardized experiments applied to the most commonly used metals including pure copper can be found in the literature (Jiang & Zhang, 2008). In Figure 2.1 is presented an schematic view of a representative Cyclic Stress Strain (CSS) response of ETP copper under strain-controlled fully reversed uniaxial loading at constant amplitude. In every cycle, the increase of maximum stress observed, effect denoted as cyclic hardening, depends on the loading magnitude and history. When cyclic hardening ceases after several cycles, a saturation state and a stable stress-strain cycle is reached. Depending on the strain amplitude $\Delta\varepsilon/2$, different values for the saturated stress amplitude $\Delta\sigma/2$, are measured; this dependency is denoted as strain range effect or non-massing behavior.

Cyclic behavior of copper is strongly dependent of the internal microstructure, and the presence of dislocations in its lattice structure. These dislocations are not randomly distributed in the material, but organized forming boundaries surrounding regions with relatively few dislocations called grains. Crystals on either side of a dislocation boundary are slightly rotated with respect to each other (*ASM Metals Handbook, Vol. 9*, 2004), and grain size and their distribution are important factors in the mechanical behavior of copper (Luoh & Chang, 1998; Conrad, 2004).

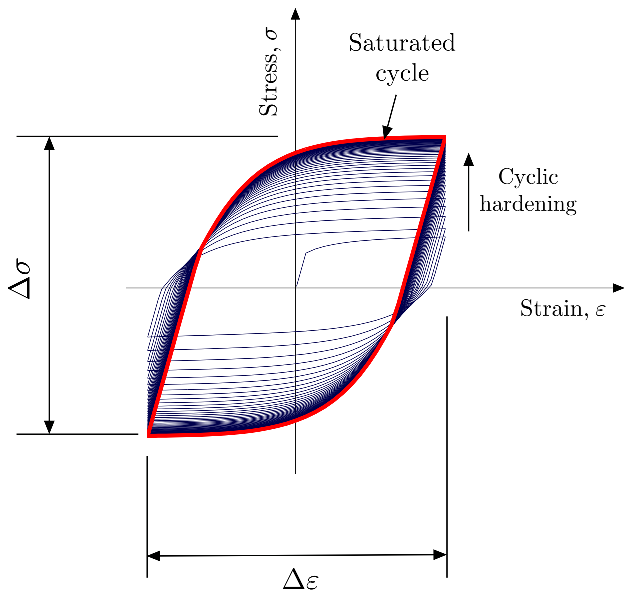

FIGURE 2.1. Schematic representation of a CSS response of ETP copper under a strain-controlled fully reversed uniaxial loading.

As copper is subjected to cycles of plastic deformation, dislocations move and new dislocations are generated forming new structures. Interactions between dislocations generate cyclic hardening, i.e., the stress range increases with an increasing number of loading cycles (Figure 2.1). This new structure of dislocations is strongly dependent on the amplitude of the imposed strain. For instance, for small strain amplitudes ($\varepsilon < 10^{-4}$) a loose vein structure has been observed. Persistent Slip Bands (PSB) are generated for bigger strain amplitudes and a large number of cycles. Cell structures are formed at large strains (Zhang & Jiang, 2005; Moosbrugger, Morrison, & Jia, 2000). Due to these dislocation microstructure differences, cyclic hardening and saturation stress are dependent on the applied strain range, producing the macroscopically observed strain range effect. Moreover, as non proportional strain paths are imposed, i.e., multiaxial loading strain path in which a non-linear relation between axial and shear strains holds, a finer cell structure is formed and therefore an additional hardening is present in cyclic stress strain response (Zhang & Jiang, 2005), this phenomenon is denoted as non-proportional hardening.

Kinematic hardening and microstructure are also related. Back-stress is due to mechanisms at different scales, including factors such as the elastic constraint imposed by hard regions over soft regions, e.g., strain cells walls over channels, heterogeneity of slip systems generating soft and hard volumes, and grains with harder orientations relative to other deforming grains (Moosbrugger et al., 2000). The grain size distribution also affects internal stresses, which are responsible of kinematic hardening (Berbenni, Favier, & Berveiller, 2007).

As a consequence of the previously explained microscopical damage generated by plastic deformation, the macroscopical properties of cold-worked copper, such as fatigue life and ductility, are downgraded. In order to restore these properties, which are essential for an energy dissipation device to work properly, cold-worked copper should be annealed. The annealing process comprises the stages of *recovery*, *recrystallization*, and *grain growth* (*ASM Metals Handbook, Vol. 9*, 2004). In the early stages of annealing, as temperature is applied, the *recovery* process produces annihilation and rearrangement of dislocations; as the thermal treatment continues, new strain-free grains are generated due to *recrystallization*; and at a final stage, *grain growth* occurs due to the instability of grain boundaries when the annealing temperature after recrystallization is sustained in time (*ASM Metals Handbook, Vol. 9*, 2004). For our case, copper test specimens and energy dissipation devices were made out of a cylindrical rod of cast ETP copper, and after the mechanization process, the elements were annealed for 4 hours at $550°C$.

3. CONSTITUTIVE MODEL OF ETP COPPER

3.1. Model Selection

Metallic dampers base their energy dissipation capacity on the inelastic cyclic characteristics of the base metal. At a macroscopical level, the shape of the cyclic response and the cyclic hardening (or softening for some metals), can be represented mathematically by elasto-plastic models. These models are based on the use of a yield surface in the stress space, which separates the elastic and plastic domains. When the stress state is inside the yield surface, no plastic flow occurs, when the stress state is in the surface and its increment is pointing outward from the yield surface, plastic flow take place. If the model includes hardening, when plastic flow occurs, the yield surface is translated (kinematic hardening), expanded (isotropic hardening), or both, according to the hardening rules of the model (Figure 3.1).

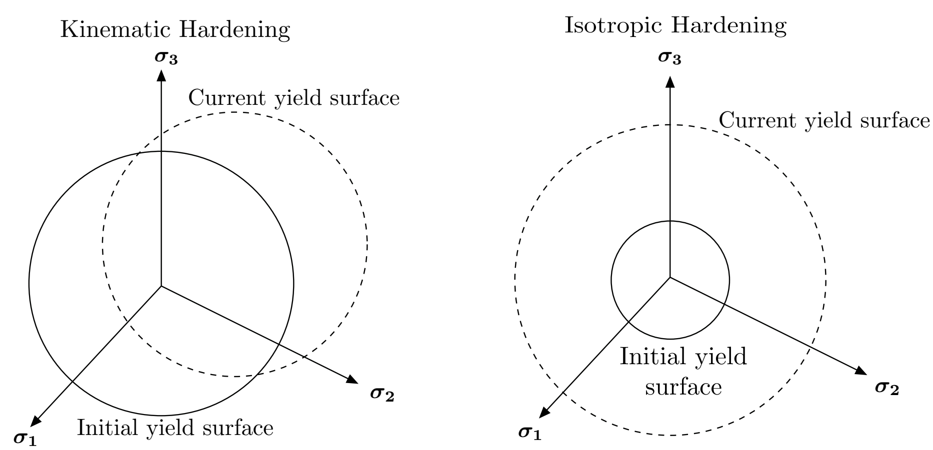

FIGURE 3.1. Schematic representation in the stress space of the kinematic and isotropic hardening.

A non-linear kinematic hardening rule, which uses only the yielding surface, has been developed by Chaboche (Chaboche, 1986). This kinematic hardening rule can be superimposed with an isotropic hardening rule to take into account the cyclic hardening experimentally observed (Figure 2.1). The strain range dependence of the isotropic hardening and saturation can also be represented by the introduction of the memory surface defined in plastic strain space, which keeps track of the maximum strain range experienced by the material and changes its position and size as the maximum plastic strain changes. The stress range in the saturated state depends on the size of the memory surface, which is proportional to the maximum strain range reached by the material on the previous loading.

Further work has been done to enhance the Chaboche model in order to include other cyclic effects of metals, such as non-proportional hardening, and viscoplastic effects (Chaboche, 2008). The Chaboche model can also be modified to predict the characteristic plateau of the response of carbon steel using a modified memory surface (Ucak & Tsopelas, 2011).

3.2. Chaboche model general equations

Assuming that elastic strains are small relative to the plastic ones, an additive decomposition of the strain rate into elastic and plastic components, $\dot{\boldsymbol{\varepsilon}_e}$ and $\dot{\boldsymbol{\varepsilon}_p}$, is customarily assumed

$$\dot{\boldsymbol{\varepsilon}} = \dot{\boldsymbol{\varepsilon}_e} + \dot{\boldsymbol{\varepsilon}_p} \tag{3.1}$$

and according to the Von Mises yielding criterion, the yield function F is defined as

$$F = \left(\frac{3}{2}(\boldsymbol{S} - \boldsymbol{\alpha}) : (\boldsymbol{S} - \boldsymbol{\alpha})\right)^{1/2} - R(p) \tag{3.2}$$

where $\boldsymbol{S}$ is the deviatoric stress tensor; $\boldsymbol{\alpha}$ is the stress tensor defining the origin of the yield surface, defined by $F = 0$; and R is a scalar variable defining the size of the yield surface, and it depends on the accumulated plastic strain, p. The double-dot represents an inner tensorial product.

Plastic flow only occurs when $F = 0$ and $(\partial F/\partial \boldsymbol{S} : \dot{\boldsymbol{S}}) > 0$, which means that the stress state is on the yield surface and its increment is pointing outward from the yield surface. Assuming the classical normality hypothesis, and an associated flow, the direction of the plastic strain increment points in the outward normal direction of the yield surface, and hence, the behavior of $\dot{\boldsymbol{\varepsilon_p}}$ is determined by

$$\dot{\boldsymbol{\varepsilon_p}} = \boldsymbol{\lambda}\frac{\partial F}{\partial \boldsymbol{S}} = \frac{3}{2}\lambda\frac{\boldsymbol{S}-\boldsymbol{\alpha}}{R} \tag{3.3}$$

where λ is the plastic multiplier, which in this case, due to the Von Mises yielding criterion, is equivalent to the accumulated plastic strain increment $\dot{p} = \lambda = (\frac{2}{3}\dot{\boldsymbol{\varepsilon}}_p : \dot{\boldsymbol{\varepsilon}}_p)^{1/2}$. The variable $\boldsymbol{\alpha}$ in Equation 3.2, namely the back stress, controls the kinematic hardening of the model by defining the center of the yield surface in the deviatoric stress space. Its value results from the superposition of two or more variables ($N = 2$ in our case), and it follows the differential equation(Chaboche, 1986)

$$\dot{\boldsymbol{\alpha}} = \sum_{i=1}^{2}\dot{\boldsymbol{\alpha}}_i = \sum_{i=1}^{2}\left(\frac{2}{3}C_i\dot{\boldsymbol{\varepsilon}_p} - \gamma_i\boldsymbol{\alpha}_i\dot{p}\right) \tag{3.4}$$

where C_i and γ_i are constants that are calibrated for different materials.

In the unidimensional case, α is a scalar, and Equation 3.4 can be integrated assuming that there is no isotropic hardening. The resulting curve, schematically depicted in Figure 3.2, shows that the maximum possible value of α is the sum of the ratios C_i/γ_i, and the rate of hardening for each α_i is γ_i.

3.2.0.1. Isotropic hardening

The cyclic hardening observed in the copper experiments can be modeled as isotropic hardening, that is, the change in the yield surface size R depends on the accumulated plastic strain p. The inconvenience with this approximation is that the shape of the cycles is scaled but preserved, which is not the case in real cycles. In order to account for the

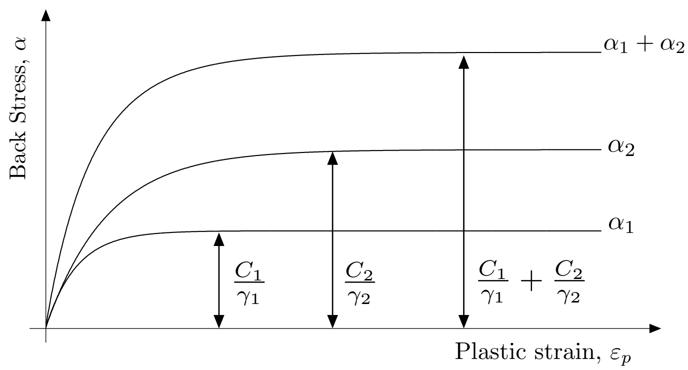

FIGURE 3.2. Schematic illustration showing the behavior of α versus plastic strain ε_p in the unidimensional case, and the role of the kinematic hardening parameters.

change in both, the shape of the CSS response and the stress range due to cyclic strain-controlled loading (Figure 2.1), the variables C_i, defined in Equation 3.4, and R can be both redefined as dependent of the accumulated plastic strain p. Therefore, the evolution equation of the kinematic hardening parameter $C_i(p)$ is (Lemaitre & Chaboche, 2000)

$$C_i(p) = C_i^{\infty}(1 + (k-1)e^{-wp}) \tag{3.5}$$

where C_i^{∞},k, and w are material dependent parameters. Shown in Figure 3.3 (a), is an schematic representation of the function $C_i(p)$. If p is large, C_i approaches C_i^{∞} asymptotically, and if p is zero, it approaches kC_i^{∞}. The rate of transition is controlled by parameter w.

The evolution of parameter $R(p)$, controlling the size of the yield surface, is determined by

$$R(p) = R_0 + Q(1 - e^{-bp}) \tag{3.6}$$

where R_0, b, and Q are material parameters which are constant in the case of isotropic hardening and no strain range effect. A schematic representation of Equation 3.6 is shown in Figure 3.3 (b). As p takes large values, the size of the yield surface grows asymptotically to a limit of $Q + R_0$, reaching saturation. Otherwise, if p is zero, R starts at R_0, which is the initial size of the yield surface. The rate of growth of $R(p)$ is defined by the dimensionless parameter b.

The exponential functions of Equations 3.5 and 3.6 enable us to describe properly the saturation of the stress-strain response observed (Figure 2.1) and its relationship with the accumulated plastic strain p. When a cyclic strain-controlled loading is imposed, p increases and the response reaches saturation, in which the variables $R(p)$ and $C_i(p)$ become constant and the contribution of isotropic hardening is bounded in the response, remaining the kinematic hardening active.

From the consistency rule under yielding $dF = 0$, the classical normality hypothesis (Equation 3.3), and the kinematic and isotropic hardening rules (Equations 3.4 and 3.6), the plastic multiplier λ is (Lemaitre & Chaboche, 2000)

$$\lambda = \frac{1}{h} H(F) \left\langle \frac{\frac{3}{2}(\boldsymbol{S} - \boldsymbol{\alpha}) : \dot{\boldsymbol{S}}}{R} \right\rangle \tag{3.7}$$

$$h = \sum_{i=1}^{2} \left(C_i - \frac{\frac{3}{2}\gamma_i \boldsymbol{\alpha} : (\boldsymbol{S} - \boldsymbol{\alpha})}{R} \right) + b(Q - (R - R_0)) \tag{3.8}$$

where h is denoted as the hardening modulus; $H(F)$ stands for the Heaviside function of the yield surface, i.e., $H(F) = 0$ if $F < 0$, and $H(F) = 1$ if $F \geq 0$; and the chevron brackets are defined as $< x >= xH(x)$. Using this definition of the Heaviside function and the chevron brackets, the yielding rule is automatically incorporated, due to the fact that when the stress state is inside the yield surface $H(F) = 0$, and no plastic deformation is induced, meaning that the material is in an elastic regime. The same result is obtained when the stress state is on the yielding surface ($F = 0$) and the increment of deviatoric stress $\dot{\boldsymbol{S}}$ is pointing inwards to the yield surface, meaning that the material is subjected to unloading.

In order to include the strain range effect in this model, the saturation stress Q needs to depend on the strain range (Chaboche, 1986). The strain range can be recorded using a new surface denoted as a memory surface, which is defined in the plastic strain space by the function

$$f = \left(\frac{3}{2}(\boldsymbol{\varepsilon}_p - \boldsymbol{\xi}) : (\boldsymbol{\varepsilon}_p - \boldsymbol{\xi})\right)^{1/2} - q = 0 \tag{3.9}$$

where q is the size of the memory surface, which represents the maximum plastic strain range in a multiaxial loading case; and $\boldsymbol{\xi}$ represents the center of the surface. Changes in the surface size and position take place only if the plastic strain is on the surface $f = 0$, and the plastic strain increment is pointing outwards from the memory surface, i.e., $(\partial f/\partial \boldsymbol{\varepsilon_p}) : \dot{\boldsymbol{\varepsilon_p}} > 0$. The following equation determines the evolution of the memory surface size q (Chaboche, 1986)

$$\dot{q} = \frac{1}{2}H(f) < \boldsymbol{n} : \boldsymbol{n}^* > \dot{p} \tag{3.10}$$

where $H(f)$ stands for the Heaviside function of the memory surface; and $\boldsymbol{n}$ and $\boldsymbol{n}^*$ are the outward unit normals of the yield surface and the memory surface, respectively

$$\boldsymbol{n} = \frac{\frac{\partial F}{\partial \boldsymbol{S}}}{(\frac{\partial F}{\partial \boldsymbol{S}} : \frac{\partial F}{\partial \boldsymbol{S}})^{1/2}} = \sqrt{\frac{3}{2}}\frac{\boldsymbol{S} - \boldsymbol{\alpha}}{R + R_0} \tag{3.11}$$

$$\boldsymbol{n}^* = \frac{\frac{\partial f}{\partial \boldsymbol{\varepsilon_p}}}{(\frac{\partial f}{\partial \boldsymbol{\varepsilon_p}} : \frac{\partial f}{\partial \boldsymbol{\varepsilon_p}})^{1/2}} = \sqrt{\frac{3}{2}}\frac{\boldsymbol{\varepsilon_p} - \boldsymbol{\xi}}{q} \tag{3.12}$$

The increment of the memory surface central position $\dot{\boldsymbol{\xi}}$, can be calculated as

$$\dot{\boldsymbol{\xi}} = \frac{1}{2}\sqrt{3/2}H(f) < \boldsymbol{n} : \boldsymbol{n}^* > \boldsymbol{n}^*\dot{p} \tag{3.13}$$

The evolution of the saturation stress $Q(q)$, now dependent of the memory surface size q, is defined by

$$\dot{Q} = 2\mu(Q_s - Q)\dot{q} \tag{3.14}$$

where μ and Q_s are material constants, which are calibrated experimentally. Integration of Equation (3.14) leeds to

$$Q(q) = Q_s + (Q_0 - Q_s)e^{-2\mu q} \tag{3.15}$$

which functional shape is depicted in Figure 3.3 (c). It is apparent that as the strain range q becomes large, the saturation stress Q increases asymptotically to Q_s. Therefore, for large strain the isotropic hardening saturates at higher stress values than for small strain. If no plastic strain is applied, then q is zero and $Q(0) = Q_0$, which is the initial saturation stress. The parameter μ defines the rate of increase of the saturation stress. A summary of the main equations of the presented model is shown in Table 3.1.

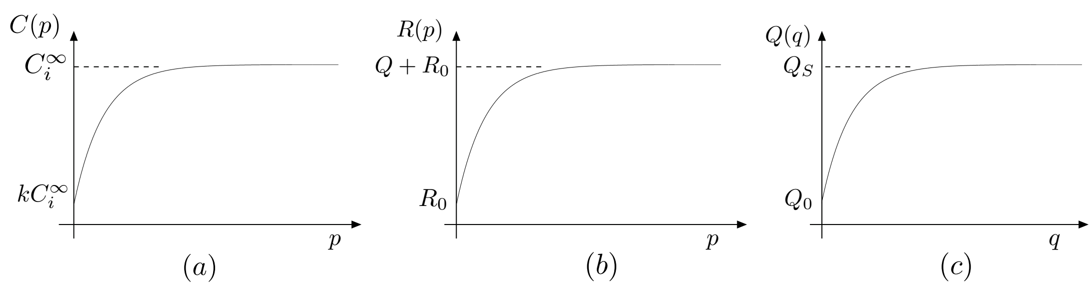

FIGURE 3.3. Functional variations of constitutive model parameters: (a) Relationship between yield surface size R and accumulated plastic strain p; (b) Schematic variation of the kinematic parameter $C_i(p)$ as a function of p, for different values of the material constant k; (c) Relationship between saturation stress Q and memory surface size q.

3.3. Unidimensional case

The unidimensional case of the Chaboche constitutive model just described was programmed using Matlab (Matlab, 2010). The purpose is to fit the material parameters for ETP copper using the experimental data from uniaxial strain-controlled tests. In order to validate the programmed Matlab subroutine, the cyclic response was obtained

TABLE 3.1. Main equations of the Chaboche model with memory effect.

Yield surface	$F = \left(\frac{3}{2}(\boldsymbol{S} - \boldsymbol{\alpha}) : (\boldsymbol{S} - \boldsymbol{\alpha})\right)^{1/2} - R(p) = 0$
Kinematic hardening	$\dot{\boldsymbol{\alpha}} = \sum_{i=1}^{2} \left(\frac{2}{3} C_i(p) \dot{\boldsymbol{\varepsilon}}_p - \gamma_i \boldsymbol{\alpha}_i \dot{p} \right)$
Isotropic hardening	$C_i(p) = C_i^{\infty}(1 + (k-1)e^{-wp})$ $R(p) = R_0 + Q(1 - e^{-bp})$
Memory surface	$f = \left(\frac{3}{2}(\boldsymbol{\varepsilon}_p - \boldsymbol{\xi}) : (\boldsymbol{\varepsilon}_p - \boldsymbol{\xi})\right)^{1/2} - q = 0$ $\dot{q} = \frac{1}{2} H(f) < \boldsymbol{n} : \boldsymbol{n}^* > \dot{p}$ $\dot{\boldsymbol{\xi}} = \frac{1}{2}\sqrt{3/2} H(f) < \boldsymbol{n} : \boldsymbol{n}^* > \boldsymbol{n}^*$
Strain range effect	$Q(q) = Q_s + (Q_0 - Q_s)e^{-2\mu q}$

for randomly chosen material parameters using six different strain inputs. The response was compared with results from a finite element model using the open source software Code_Aster (Code Aster, 2008), which has the same constitutive model implemented for the general three-dimensional case. A very good match was obtained between models as shown in Figure 3.4.

3.4. Identification of ETP copper parameters

The parameter identification for ETP copper was performed using the Matlab subroutine, assuming that the parameters thus obtained would still be valid for the 3D-case. The identification process was conducted following the recommendations of Chaboche (Chaboche, 1986), which uses a set of fully reversed strain-controlled uniaxial tests at constant amplitude. Nine uniaxial tests were performed on ETP copper coupons using the 8872 Instron Fatigue Testing System, and a 3542 Axial Epsilon Extensometer (Figure 3.5). The test coupons were made by a mechanization process from a cylindrical rod, and afterwards underwent an annealing process at $550°C$ for 4 hours, in order to restore their initial mechanical properties. The applied strains were in cycles at constant amplitude,

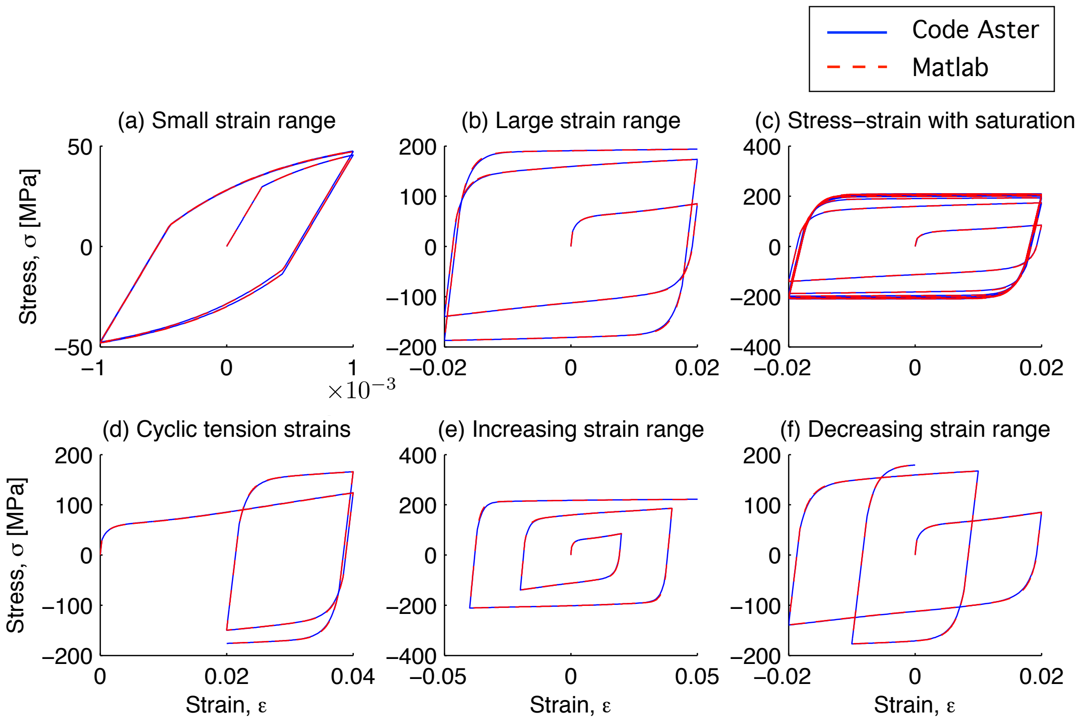

FIGURE 3.4. Numerical evaluation between Matlab and Code Aster for an uni-dimensional case with randomly chosen material parameters.

and repetitions were performed until saturation was reached (Figure 2.1) for each test. Shown in Figure 3.5 is the test coupon geometry and the experimental setup for the tests performed.

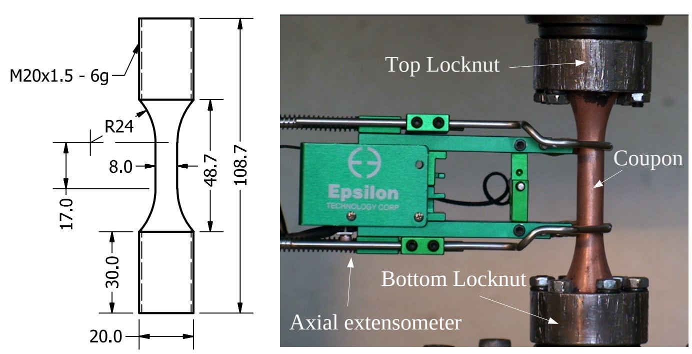

FIGURE 3.5. Experimental setup and sketch of test coupons.

Chaboche's constitutive model requires the identification of ten parameters. The process starts with the identification of the memory-effect parameters, and then with the isotropic and kinematic hardening parameters, assuming that the memory-effect parameters are known.

Shown in Figure 3.6 (a), is the cyclic stress-strain response of one ETP copper coupon under a fully-reversed strain loading. Initially, the yield stress is very low, $R_0 = 20$ MPa, and after 20 cycles, the response reaches a saturation state, in which the stress range and the shape of the cycles remain unchanged. From the saturated state, the saturation yield stress R_{sat}, and the copper Young Modulus E_{Cu}, are measured. As the stress-strain relationship reaches a saturated state, the final yield stress R_{sat} can be derived from Equation 3.6, i.e.,

$$R_{sat} = \lim_{p\to\infty} R(p) = R_0 + Q \implies Q = R_{sat} - R_0 \tag{3.16}$$

and the saturation stress is calculated directly from subtraction.

Shown in Figure 3.6 (b) are the final cycles recorded at saturation of the nine tests performed, which referred to a common origin. The saturated cycle shown using dashed line corresponds to the test shown in Figure 3.6 (a). This configuration makes evident that the curves do not have the same yield stress value at saturation, and therefore the saturated response depends on the applied strain range. For each of these curves, R_{sat} can be measured, and using this value, the saturation stress Q can be computed from Equation 3.16. The applied plastic strain range in each test can be calculated as follows

$$q = \Delta\varepsilon/2 - \frac{\Delta\sigma/2}{E_{Cu}} \tag{3.17}$$

These nine experimental points of the saturation stress Q_j and plastic strain range q_j can be used to identify the memory surface parameters Q_0, Q_s and μ present in Equation 3.14, by solving the following least square minimization problem

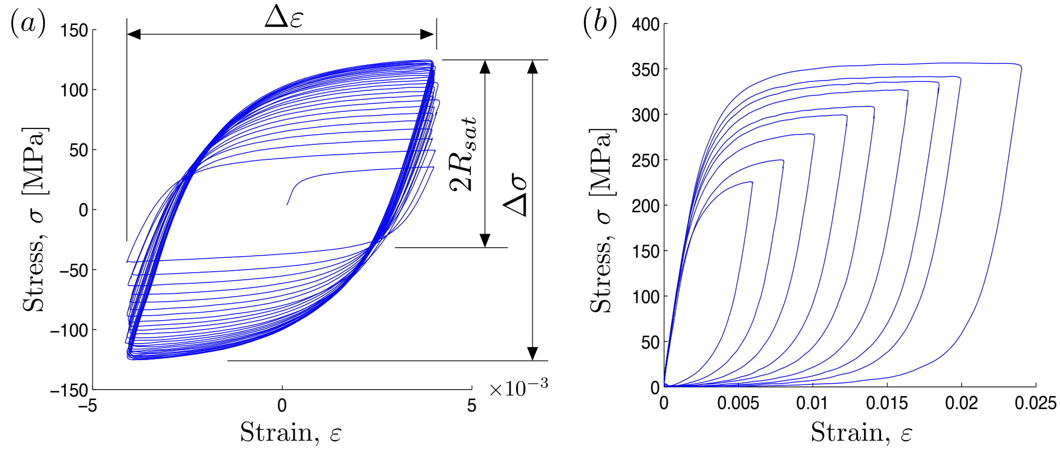

FIGURE 3.6. Cyclic stress-strain (CSS) response of ETP copper under fully-reversed cyclic loading: (a) CSS curve for a cycle strain range $\Delta\varepsilon/2 = 0.004$; (b) CSS curves of the nine performed tests at saturation.

$$\min_{Q_0, Q_S, \mu} \left[\sum_{j=1}^{9} Q(q_j) - Q_j \right] \tag{3.18}$$

where $Q(q_j)$ represents the numerical value of saturation stress calculated from Equation 3.14 for the j-th test. Shown in Figure 3.7, are both, the experimental points (q_j, Q_j), and the theoretical curve $Q(q)$ calculated from Equation 3.14 using the identified parameters, which are sumarized in Table 3.2.

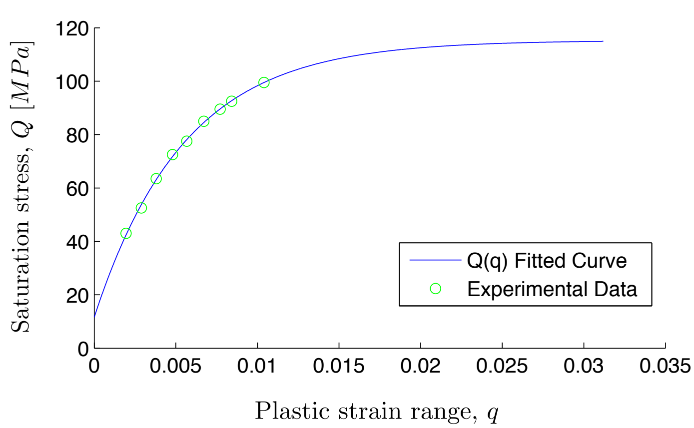

FIGURE 3.7. Identification of memory effect parameters Q_0, Q_s and μ.

The identification of the kinematic model parameters $C_1^{\infty}, \gamma_1, C_2^{\infty}, \gamma_2$, and the isotropic hardening parameters b, k, w, was performed using the experimental CSS curve shown in Figure 3.8 (a), obtained from a cycle strain-controlled test at a constant deformation amplitude $\Delta\varepsilon/2 = 0.04$. The Matlab routine of the stress-strain constitutive model in the unidimensional case, assuming that the identified memory effect parameters are set, is used to obtain the material parameters, by solving the least square minimization problem

$$\min_{C_1^{\infty}, \gamma_1, C_2^{\infty}, \gamma_2, b, k, w} \left[\sum_{k=1}^{n} \sigma(\varepsilon_k^{\exp}) - \sigma_k^{\exp} \right] \tag{3.19}$$

where $\sigma_k^{\exp}$ are the experimental values of the CSS curve; $\sigma(\varepsilon_k^{\exp})$ represents the numerical stress-strain curve obtained using Matlab; and n is the total number of experimental values. The numerical CSS curve, obtained using the identified parameters, is shown in Figure 3.8 (b). The response exhibits excellent agreement with the experimental curve in terms of isotropic hardening, saturation process, and loop shape.

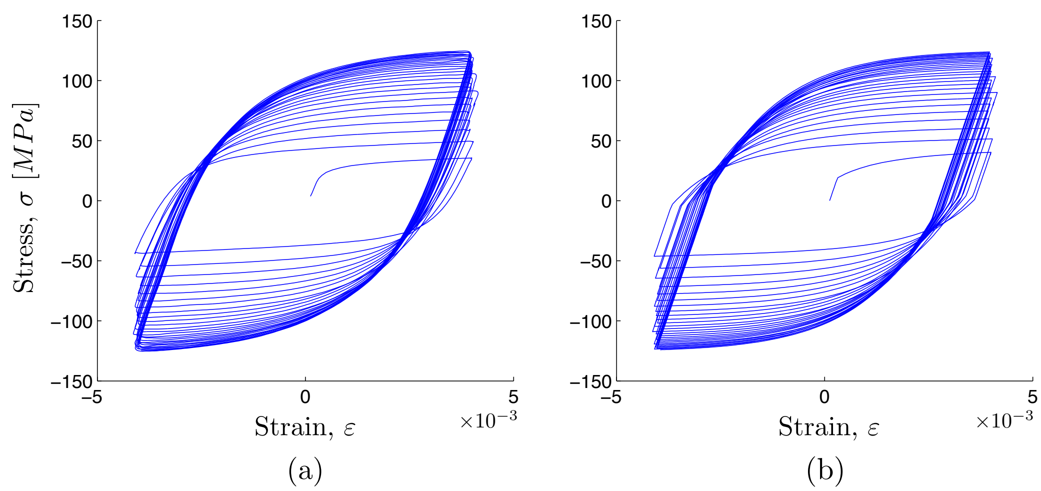

FIGURE 3.8. Comparison between stress-strain constitutive models of copper test coupon shown in Figure 3.5: (a) experimental stress-strain curve under a fully reversed cycle at $\Delta\varepsilon/2 = 0.04$; and (b) numerical cyclic stress-strain curve corresponding to $\Delta\varepsilon/2 = 0.04$.

The identified parameters, summarized in Table 3.2, were used to calculate the response at saturation of the nine tests performed, which were compared with the experimental ones, as shown in Figure 3.9. The model proves to be very accurate in the representation of both, the stress range and the shape of the saturated cycles.

TABLE 3.2. Identified parameters for the tested ETP copper coupons (Figure 3.5).

Cu-Elastic parameters		Cu-Kinematic hardening parameters (Equation (3.4))			
E/GPa	R_0/MPa	C_1^∞/MPa	γ_1	C_2^∞/MPa	γ_2
101.4	20	26930	700	39302	2291
Cu-Isotropic hardening and memory effect parameters (Equations (3.5), (3.6), (3.15))					
Q_0/MPa	Q_S/MPa	μ	b	k	w
10	116	90.9	5.9	0.4	14.0

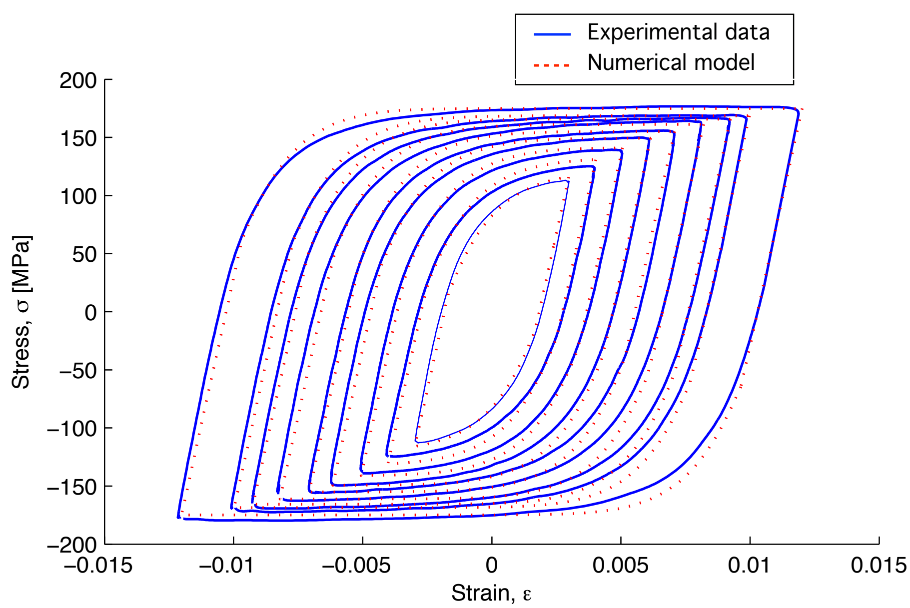

FIGURE 3.9. Comparison between the experimental stress-strain curves at saturation of a copper coupon (Figure 3.5) and results from the numerical model.

4. FINITE ELEMENT MODEL OF THE CUBEDD

4.1. Model description

Shown in Figure 4.1 (a) is a schematic longitudinal section of the proposed Cu-BEDD device and the definition of the seven parameters that describe its geometry. Four of the seven parameters shown were selected to investigate the optimal shape of the device: its height, H, the largest and smallest diameter D and d, respectively, and the thickness of the conical shape, e. The other three parameters, i.e., the radii of curvature R and r, and the height of the solid nucleus, h, are essentially meant to avoid stress concentrations and, though important in the design, do not have a strong effect on the energy dissipating capacity of the device.

The model was developed using the finite element open source software, Code Aster (Code Aster, 2008), considering large deformations and the Chaboche constitutive model just described, using the identified material parameters. The FE mesh included three or more quadratic tetrahedral elements across the thickness of the cone shaped part of the device to correctly represent the gradient of the stress field, which is the part that undergoes larger plastic deformation during bending. The rest of the mesh was generated considering a maximum element dimension of 3 mm; a longitudinal section of a typical FE mesh of the Cu-BEDD is shown in Figure 4.1 (b).

The boundary conditions for the analysis of the device are presented in Figure 4.1 (c). The conditions are defined by zero displacement of each node at the bottom of the device. At each node at the top of the device, there is no displacement in both, the vertical direction and the perpendicular direction to the plane shown for the device. The imposed displacement occurs in the horizontal direction as shown by the arrow in Figure 4.1 (c).

In order to optimize the shape of the device at a less computational cost, a simpler model was developed using Ansys (Ansys Inc., 2009). The simplified model includes also large deformations, and has the same mesh parameters and boundary conditions as the one developed in Code Aster; the only difference lies in the constitutive model, which considers kinematic and isotropic hardening, without memory effects.

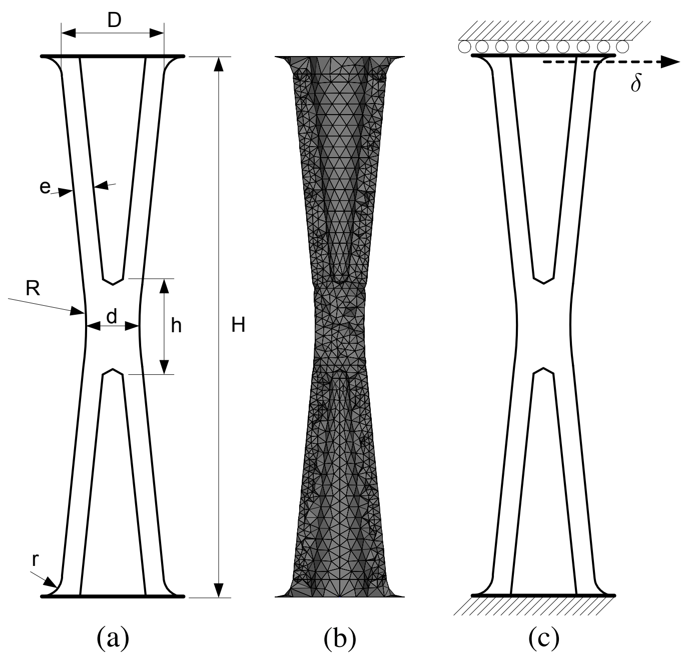

FIGURE 4.1. Geometry definition of the Cu-BEDD device and the FE model: (a) definition of geometry and parameters; (b) longitudinal section of the FE mesh; and (c) boundary conditions imposed into the model.

4.2. Design of the device

In order to obtain a geometric design of the Cu-BEDD, its response to cyclic loading, has to meet two main requirements: (1)To have a stable and a large energy dissipating force-deformation cycles, at the minimal cost possible; and (2) to endure in a stable manner at least the number of deformation cycles imposed in one strong earthquake.

In order to accomplish the above mentioned requirements, an initial hourglass-like shape was adopted. In the past, an hourglass shape has been obtained from a shape optimization in the case of a metal plate subjected to in-plane bending (Kobori et al., 1992); it has the desirable property of maximizing the energy dissipated due to plastification when it is deformed. A prior bi-directional energy dissipation device was also developed using an hourglass shape proving to have an outstanding performance (Kobori et al., 1992). Due to the fact that plastification takes place mostly in the zones close to the exterior surface of the device, the adopted hourglass shape was complemented with two conical holes (Figure 4.1 (a)) to minimize the copper weight without having a strong impact on the energy dissipation capacity of the device.

To obtain optimal values for the geometric parameters h, D, d, and e, the approach was to select and test several device configurations (with different geometric parameter values) and fit a hyper surface for the available responses. From this response surface, an optimal value of the geometric parameters can be obtained by optimization of the response, in which the response is maximized or minimized according to the design requirements. Such an approximation belongs to the Response Surface Methodology, (Pukelsheim, 2006), in which the experimental tests were replaced with numerical data obtained using the FE model. A device with the final design was manufactured and tested in order to validate it by ensuring the fulfillment of the design requirements. The response maximized was the dissipated energy density, $\bar{E}_{dis} = E_{dis}/W$, where W represents the weight of the device. For the sake of numerical efficiency, the imposed lateral displacement consisted in just one full sinusoidal cycle at constant amplitude; 10 and 15 mm amplitudes were considered for the design of the two Cu-BEDD prototypes.

According to standards, at least five fully-reversed cycles at maximum earthquake amplitude are required (SEI/ASCE 7-05, 2006). To ensure such requirement, and due to the fact that low-cycle fatigue life depends on the imposed strain amplitude, a cap on the maximum strain in the device is imposed. Assuming that a uniaxial case of fully-reversed tension-compresion represents approximately working conditions for the most strained parts of the Cu-BEDD, the strain amplitude for a number of cycles prior to failure, N_f, can be estimated from the strain-life curve proposed by Manson (Manson, 1965)

$$\frac{\Delta\varepsilon}{2} = \left(\frac{C}{N_f}\right)^{\frac{1}{\nu}} + \varepsilon_0 \tag{4.1}$$

where C and ν are both material constants in the the strain-life baseline equation; ε_0 is interpreted as the strain limit below which fatigue damage is minimal (Jiang, 2000); and $\Delta\varepsilon/2$ is the strain amplitude. Substituting in Equation 4.1 the parameters obtained for pure copper (Zhang & Jiang, 2006) ($\nu = 2.1$, $C = 0.035$, $\varepsilon_0 = 0.00045$, and $N_f = 20$), one gets the maximum strain amplitude allowed for the test as $\Delta\varepsilon/2 \simeq 0.049$. In the case of the Cu-BEDD the strain is a tensorial variable, therefore the maximum equivalent strain in the device, ε_{eq}, was used as a scalar parameter to control the cap strain in the device for each numerically obtained response. According to the Von Mises criterion, ε_{eq} is defined as

$$\varepsilon_{eq} = \left(\frac{2}{3}\boldsymbol{\varepsilon} : \boldsymbol{\varepsilon}\right)^{1/2} \tag{4.2}$$

Thus, a set of numerical experiments with different geometric parameter values and both output parameters, ε_{eq} and E_{dis}/W, were obtained. By using this set of numerical points, a quadratic response surface of ε_{eq} and E_{dis}/W was calibrated, and the maximum of E_{dis}/W was found, given the cap strain condition $\varepsilon_{eq} \leq 0.049$. The geometric parameters that give the maximum of E_{dis}/W subject to $\varepsilon_{eq} \leq 0.049$, are the ones used for the final design of the Cu-BEDD prototypes. The process was repeated for both displacement amplitudes of 10 and 15 mm. The resulting geometric parameters are shown in Table 4.1.

Shown in Figure 4.2 are contour lines of the response surface E_{dis}/W, as a function of the geometric parameters D, H, d, and e (Figure 4.1 (a)), for a displacement demand $\delta = 10\ mm$. The hyper surface depends on all four parameters, but, it is plotted as a function of two, while keeping the other two parameters as shown in Table 4.1. Therefore, in the case of the surface shown in Figure 4.2 (a) the values of d, and e, were fixed, and in the case of Figure 4.2 (b), the values of D and H were fixed. Along with the response surface, the optimal value is shown by a circular dot, and the domain is subdivided by a dotted line separating the allowed zone, where $\varepsilon_{eq} \leq 0.049$, from the not allowed zone, where $\varepsilon_{eq} > 0.049$. In Figure (a), it is shown that the the response E_{dis}/W increases when

D increases and H decreases, suggesting that the ratio H/D is inversely proportional to the energy dissipated. Figure (b), shows that the the response E_{dis}/W increases when d increases and e decreases. In both cases, the optimal value is placed on the strain limit where $\varepsilon_{eq} = 0.049$, rather than the maximum value of the response E_{dis}/W, therefore, the limit of strain, due to the minimal low-cycle fatigue life requirement, has a strong influence on the Cu-BEDD final design.

TABLE 4.1. CU-BEDD design for two different displacement demands, δ.

Geometry	δ/mm	H/mm	D/mm	d/mm	e/mm
A	10	144.2	49.5	18.9	7.3
B	15	190.0	50.0	19.0	7.0

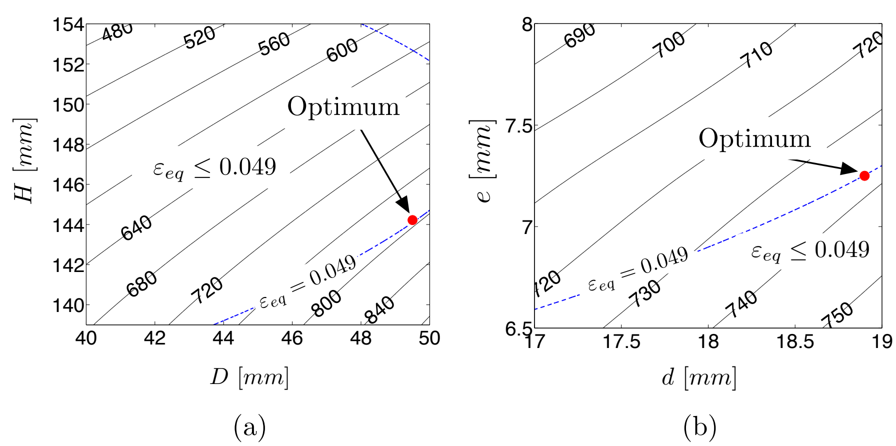

FIGURE 4.2. Response surface E_{dis}/W and optimal value of a Cu-BEDD designed for a displacement demand, $\delta = 10$ mm: (a) E_{dis}/W as a function of geometric parameters H, and D; (b) E_{dis}/W as a function of geometric parameters d, and e.

The values of parameters R and r were selected to avoid stress concentrations in the device when it is deformed. If such values were too small, stress concentration would detriment the performance of the device since only a small fraction of the material would undergo plastification. The height of the solid nucleus, h, plays an important role too, due to the fact that the shear force is transmitted through the solid core in the middle of the Cu-BEDD (see Figure 4.1 (a)). If there was no solid core, the shear force would generate large deflections in the middle of the Cu-BEDD and the device would not be capable to sustain the entire seismic signal.

The two Cu-BEDD geometries obtained from the design are shown in Figure 5.1, which are denoted hereafter, geometries A and B. The main difference between them is the device aspect ratio, H/D (Figure 4.1 (a)) which turns out to be predominant in the cyclic behavior. Indeed, it is intuitive that for small H/D, shear forces take a main role as stress source, increasing strain with less deformation imposed. Otherwise, for large H/D, bending becomes the main source of strains allowing a larger deformation of the device.

5. EXPERIMENTAL RESULTS

5.1. Tested devices and experimental setup

A total of six pairs of Cu-BEDD were tested. All of them were made of ETP copper and went through annealing at $550°C$ for 4 hours. The two different geometries derived from the design results (Table 4.1), were tested; each of them is shown in Figure 5.1. Because of symmetry reasons, two specimens were tested simultaneously by an MTS 244.31 dynamic actuator with 250 kN axial load capacity, 500 mm maximum stroke, and 500 m/s maximum speed at maximum stroke. Shear displacements and forces were measured by an LVDT and a load cell along the axis of the actuator. Two strain gauges were also located in the most critically stressed points of the device according to the FE model as shown in Figure 5.1, and the temperature in the specimen at the beginning and the end of the test was measured using the Fluke 66 infrared thermometer .

The experimental set-up used to test the Cu-BEDD probes is shown in Figure 5.2. Both tested devices were placed horizontally, such that one end of each device is fixed, and the other one is connected to the actuator rod. The anchor system to the loading frame of each test specimen was particularly tricky. Two L-shaped steel sections were bolted to each side of the vertical elements of the loading frame. Each L-shaped section was connected to the one on the opposite side by a smaller L-shaped section, placed transversely to the loading frame. Two steel plates of 15 mm of thickness were connected to the transverse L-shaped sections facing each other and, in the center, a third steel plate is connected to the actuator rod. The tested Cu-BEDD were anchored to plates by two steel parts that grab the ends of the specimens, and fix them to the plate using a bolted connection (Figure 5.2). As shown in the figure, the left and right plates are fixing the ends of the specimens, and the center plate is connected to both tested Cu-BEDD. The center plate moves with the actuator rod guided by four elements made of teflon, which are connected to the L-shaped steel sections. The guiding elements restrict movement in both directions perpendicular to the actuator axis, therefore the center plate can only travel vertically with the actuator, introducing to both devices a transversal distortion. A supernut is used to prestress the threaded connection between the actuator load cell, and the center plate to prevent any slack.

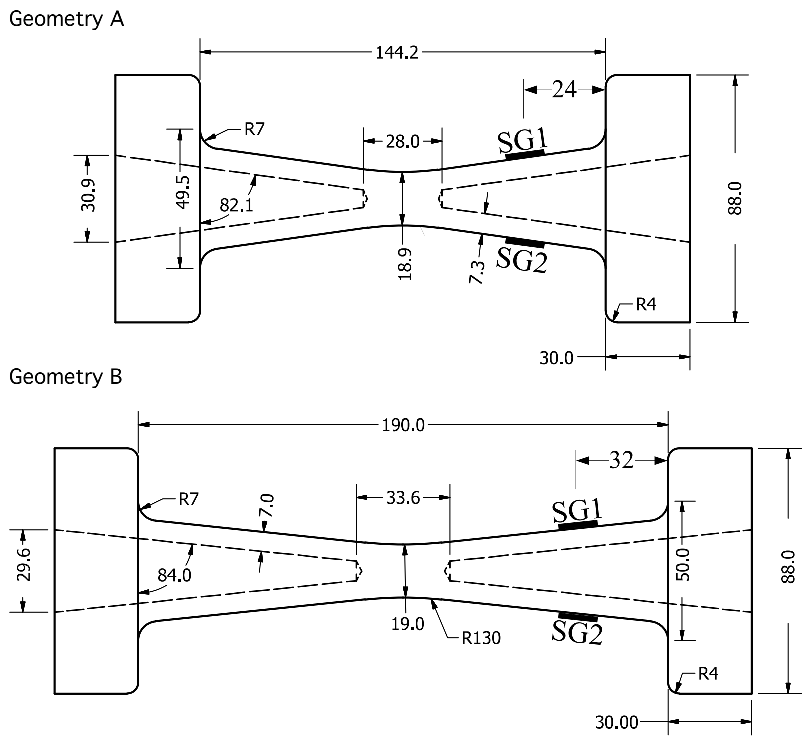

FIGURE 5.1. The Cu-BEDD prototype geometries and strain gauges position (SG1-SG2).

5.2. Experimental Results

In order to validate the FE model and the design process, two displacement-controlled tests were performed for each geometry obtained from the design. In the first test, the loading history imposed to the devices, consisted on multiple sinusoidal cycles of increasing amplitude until failure. The displacement amplitude was increased in steps, in which three sinusoidal cycles at constant amplitude were applied. This first test, allows us to have a general picture of the device cyclic behavior for several relative displacement magnitudes, and evaluate the model capability to represent such behavior.

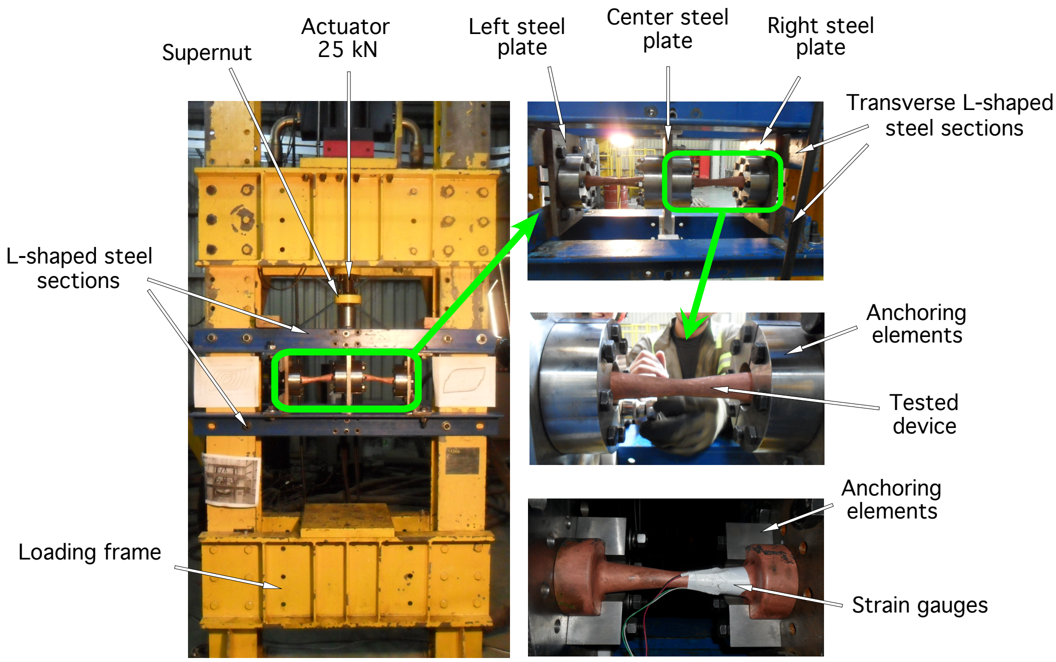

FIGURE 5.2. Sketch of Cu-BEDD probes and experimental setup: (a) devices geometry and strain gauge position (SG1-SG2); and (b) experimental setup.

In the second test, cycles of constant amplitude at the design displacement δ (Table 4.1), were performed until failure. The number of cycles to failure and the measured strain in the devices, were used to validate the design process, in which the low-cycle fatigue life was predicted using strain-controlled fully reversed uniaxial tests of pure copper. Also the force-displacement response numerically predicted, was compared to the experimentally obtained one, in order to evaluate the numerical model performance.

From the cyclic force-displacement response of the devices tested at constant imposed deformation, an efficiency factor was calculated for each test. Shown in Figure 5.3 (a), is a schematic representation of a Cu-BEDD force-displacement cycle at saturation, and superposed to the response is the rectangle defined by the maximum force and displacement developed by the device. The ratio between the enclosed area by the response of the Cu-BEDD and the area of the maximum force-displacement rectangle is denoted as the efficiency factor of the device. The rectangle area represents the maximum energy that can be dissipated in one cycle, given a maximum deformation and force; therefore the efficiency factor represents how close to that maximum value, is the energy dissipated by the device in one cycle at saturation.

In the schematic force-displacement response shown in Figure 5.3 (a) is also indicated an increase in the force towards the maximum and minimum deformations, denoted as axial effect. As schematically shown in Figure 5.3 (b), when the device is subjected to large deflections, an axial force is developed in the device due to the boundary conditions, in which no displacement of the Cu-BEDD end in the axial direction of the device is allowed. The projection of the axial force on the direction of the imposed displacement, F_{ax}, is added to the force needed to produce shear and bending, F, therefore, the total transversal force increases. In the force-deformation response of the Cu-BEDD tested, the axial effect will be observed when the device is largely distorted.

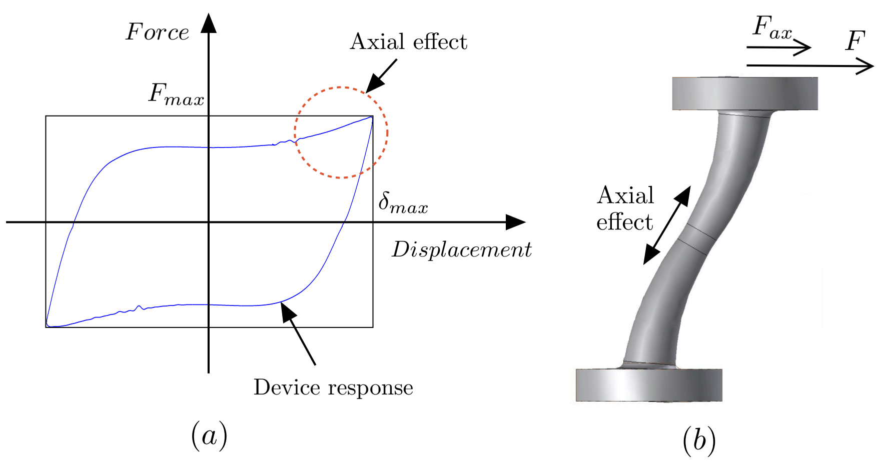

FIGURE 5.3. Definition of efficiency factor and axial effect.

Shown in Figure 5.4 (a) is the experimental force-displacement cyclic response of the device with geometry A subjected to multiple steps of increasing displacement amplitude. Every three cycles, and starting from an initial amplitude of 3.5 mm, the amplitude was increased in 2 mm until reaching failure. Results show that cycles are very stable and the maximum force increases at every cycle and at every increase of displacement, as a result of isotropic hardening of copper. The displacement at which plastic flow starts in the smaller cycle is approximately 0.3 mm, indicating that the Cu-BEDD starts dissipating energy at very small displacement amplitude. The Part (b) of the Figure 5.4 shows an equivalent cyclic response as predicted by the FE model. Agreement between model and experiment is very good. The maximum force developed by the device, $F_{max} = 1.85$ tonf, is predicted with an error of 0.1 $\%$ by the FE model, and the energy dissipated by the device through the entire test, $E_{dis} = 7434$ J, is predicted with an error of 0.9 %.

Part (c) and (d) of Figure 5.4 show the experimental and numerical results of the Cu-BEDD of geometry A for the force-displacement cycles at a constant deformation amplitude of $\delta = 10$ mm. The specimen underwent 23 cycles of amplitude 10 mm before fracture. Cycles are very stable and the force range expands for every cycle, due to isotropic hardening. The predicted cycles show excellent agreement with the experimental ones. The maximum force developed by the device, $F_{max} = 1.76$ tonf, is predicted with a 0.1 $\%$ of error, and the energy dissipated by the device through the entire test, $E_{dis} = 10908$ J, is predicted with a 0.3 % of error. The efficiency factor, measured using the cycle at saturation, is 71.7 %, which is predicted with a 0.7 % of error by the FE model. The strain in the direction in which the strain gauges were placed on the probe (Fig 5.1), was measured until the strain gauges detached from the prove at the forth cycle. The maximum strain range measured was 0.031, which is a 63 % of the maximum strain range of 0.049 obtained from the low cycle fatigue uniaxial testing of copper (Eq. 4.1). The difference in strain, is probably due to the fact that only one direction was measured by the strain gauges, and the actual value of the equivalent strain, which has to be calculated using the strain tensor, is higher. The device was designed to achieve 20 cycles before reaching fracture at a maximum equivalent strain of 4.9 %; the actual device achieved 23 cycles, which validates the design process used, and indicates that the device is capable of enduring more than one earthquake at the imposed displacement demand, $\delta = 10$ mm.

At the end of the test, the device fails due to a bending generated crack at about $H/6$ measured from the top. As shown in Figure 5.5, this location turns out to be very close to the place of maximum Von Mises equivalent strain at the end of the 23^{rd} cycle according

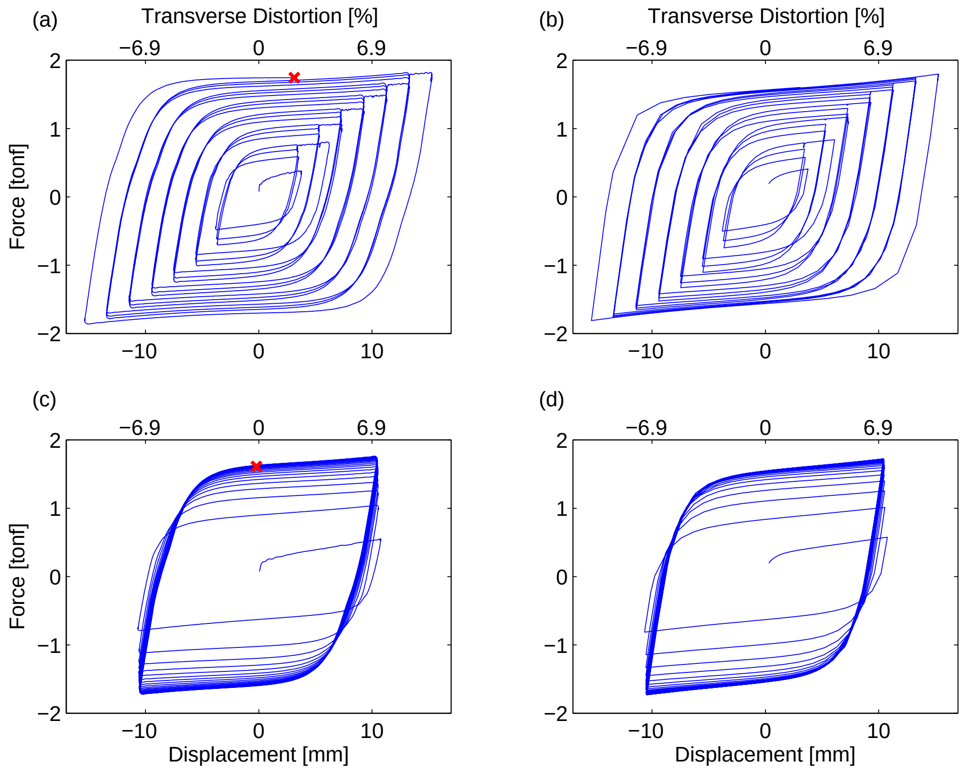

FIGURE 5.4. Experimental force-deformation cyclic response for Geometry A: (a) measured force-deformation for the cyclic test of increasing imposed deformation; (b) numerical response for increasing cyclic deformation; (c) measured force-deformation for the test performed at constant cyclic amplitude $\pm$ 10 mm; and (d) numerical response at constant cyclic amplitude.

to the FE model. Similar failure characteristics, and maximum equivalent strain location, were observed in all the other specimens tested.

Shown In Figure 5.6 are analogous results for a device with Geometry B. The measured force-deformation response for increasing imposed cyclic displacement is shown in part (a). Every three cycles, and starting from an initial displacement amplitude of 5 mm, the amplitude imposed to the device was increased in 5 mm until reaching failure. Results show that, as in the case of test of specimens with Geometry A, cycles are very stable and the force range expands for every cycle and at every increase of displacement, as a result of isotropic hardening. The equivalent predicted response shown in Figure 5.6 (b)

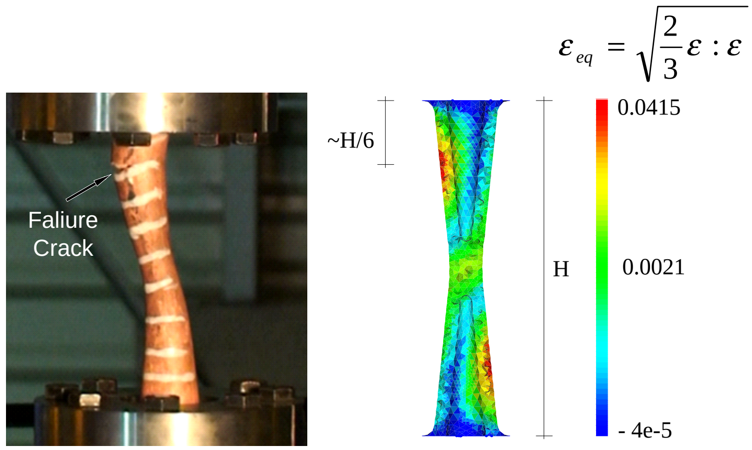

FIGURE 5.5. Position of the cracking at failure and numerical results for the Von Mises equivalent strain at the 23^{rd} cycle of constant amplitude.

presents a very good agreement with the experimental one, the maximum force developed by the device, $F_{max} = 1.34$ tonf, is predicted with an error of 14.6 % by the FE model, and the energy dissipated by the device through the entire test, $E_{dis} = 6053$ J, is predicted with an error of 7.3 %. The overestimation of the maximum force and energy dissipated, is related to an overestimation of the axial effect, which might be explained by the fact that the boundary condition of zero displacement in the longitudinal direction of the device, is not fully representative of the test conditions, in which the anchoring system is not infinitely rigid. The relative displacement at the beginning of plastification is approximately 0.5 mm, indicating that the device is capable of working in small displacement cycles. The temperature, measured at every step using the infrared thermometer Fluke 66, showed an increase of $3°K$ through the entire test, showing that the temperature is low enough to assume the copper mechanical properties remained constant throughout the test.

Parts (c) and (d) of Figure 5.6 show the experimental and numerical results of the Cu-BEDD with geometry. The force-displacement cycles were performed at a constant deformation amplitude of 15 mm. Cycles are very stable and the force range expands at every cycle, due to isotropic hardening until a saturation state is reached. The maximum force measured, $F_{max} = 1.22$ ton, is predicted with an 8.8 % of error, and the energy dissipated by the device through the entire test, $E_{dis} = 11420$ J, is predicted with an 8.1 % of error. The efficiency factor, measured from the cycle at saturation, is 71.6 %, which is predicted with a 4.8 % error by the FE model. In this case, as the equivalent test with Geomtetry A, the strain gauges detached from the probe at the seventh cycle, and the maximum strain measured one the device was 0.036. This device was designed to achieve 20 cycles before reaching fracture at a maximum equivalent strain of 4.9 %; the actual device underwent 23 cycles, validating the design process used at the imposed displacement demand, $\delta = 15$ mm.

A 33 % smaller force range was reached in this case as compared to the device of Geometry A. Also, a more prominent axial effect (Figure 5.3) is observed in the force-deformation curves, due to the larger distortions reached. The maximum force measured is a 31 % smaller, and the specific energy, E_{dis}/W, dissipated through the 23 cycles, was a 1.1 % higher relative to the tested device of Geometry A at constant deformation amplitude. A summary of the experimental results of the Cu-BEDD tested in one direction is shown in Table 5.1.

TABLE 5.1. Summary of the experimental results obtained from the Cu-BEDD tested prototypes.

Test	Geometry	Displacement Amplitude (mm)	Max Force (ton)	Specific energy dissipated (J/kg)	Efficiency (%)	Cycles to failure
Multistep	A	3.5 - 15.5	1.85	2186.5	-	19
Const. Amplitude	A	10	1.76	3208.2	71.7	23
Multistep	B	5 - 25	1.34	1681.4	-	15
Const. Amplitude	B	15	1.22	3172.2	71.6	23

In addition to the previous tests, a bi-directional test was performed on a Cu-BEDD with geometry B by imposing a cyclic deformation at an amplitude of 15 mm in two orthogonal directions. The loading direction was switched every five cycles, and results were compared to those of a single direction test. The results are shown in Figure 5.7,

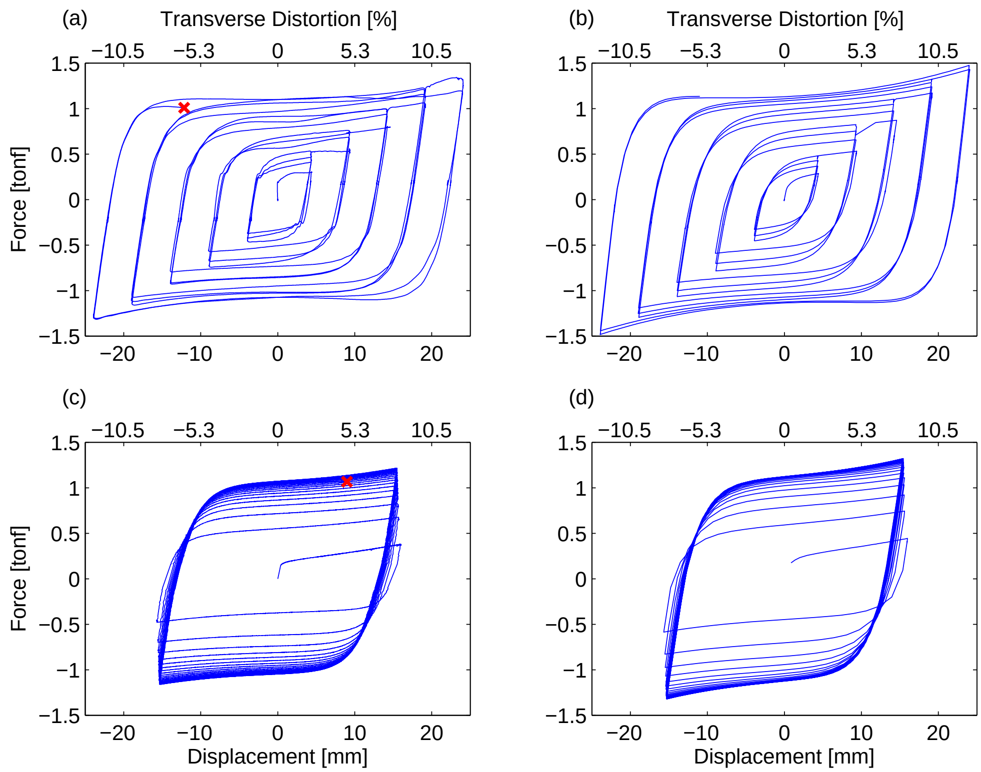

FIGURE 5.6. Experimental force-deformation cyclic response for Geometry B: (a) measured force-deformation displayed; (b) numerical response; (c) measured force-deformation displayed at constant amplitude $\pm$ 15 mm; and (d) numerical response at constant amplitude.

and include six force-displacement curves for different number of cycles, from $N = 1$ to $N = 27$. Cycle numbers indicate the sequence of the test and each row of plots corresponds to one direction of imposed deformation.

The results shown in plot 1 exhibit isotropic hardening just as the case of the single direction results shown in Figure 5.6 (a). For cycles $N = 5 - 10$, the shear force of the device starts at a higher level, and isotropic hardening is less evident in the perpendicular direction in spite of applying the same displacement amplitude. Cyclic hardening vanishes in all the following cases, which implies that isotropic hardening has been exhausted. The device collapses for N=27 at the same location as it did in the case of the unidirectional test with constant deformation amplitude, shown in Figure 5.5. The obtained maximum force is 1.19 tonf, and the energy dissipated through the entire test is 3876.1 J.

The maximum force obtained is a 2.5 % smaller relative to the unidirectional test performed on the Cu-BEDD with the same geometry, and the energy dissipated is 22 % larger, due to the changes in the loading direction. The number of cycles for the bidirectional case increased relative to the unidrectional case. However, one could think that this same device would have experienced a larger number of cycles, because plastic flow in the specimen spreads out in the entire volume of the cone shaped parts, due to the switch of loading direction. Actually, from the force-deformation curves, it is observed that after the first switch of direction, the device exhibits an already hardened behavior, which suggest that the entire cone shaped parts undergo plastic flow wether the device is subjected to a single directional or a bi-directional loading, and therefore the device behavior is not hardly sensitive to changes in the loading direction.

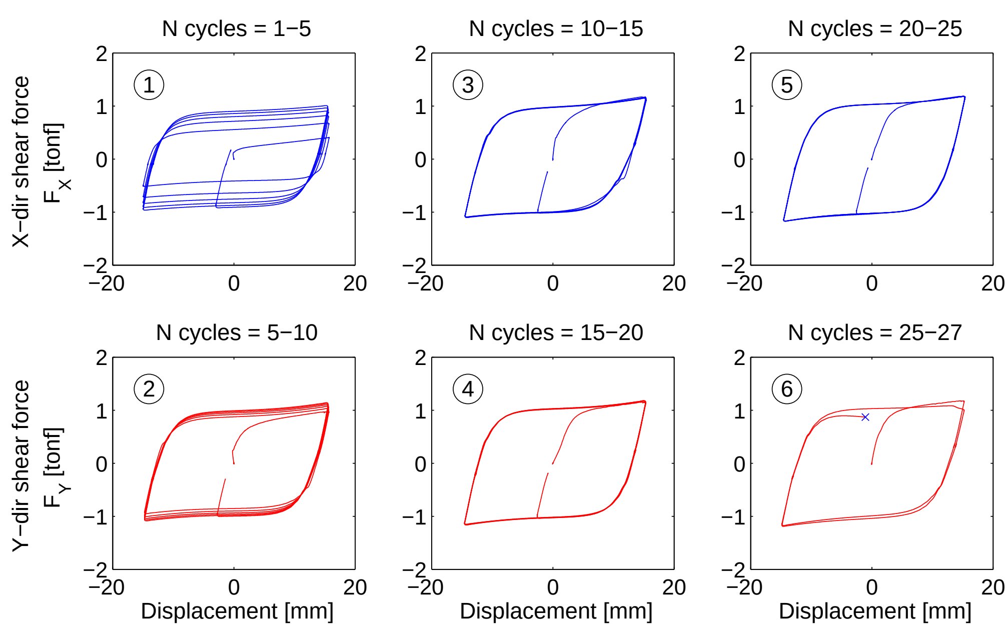

FIGURE 5.7. Force-deformation cycles of bi-directional test results of Cu-BEDD with geometry B.

Shown in figure 5.8 are the numerical results of the same bidirectional test as shown in Figure 5.7. The six curves follow the exact same order as those presented in Figure 5.7. The model proposed represents the bidirectional behavior and hardening with very good accuracy. The numerical model predicts a maximum force $13.9\ \%$ larger than the measured in the force-deformation response, and the energy dissipated is predicted with a $9.6\ \%$ of error.

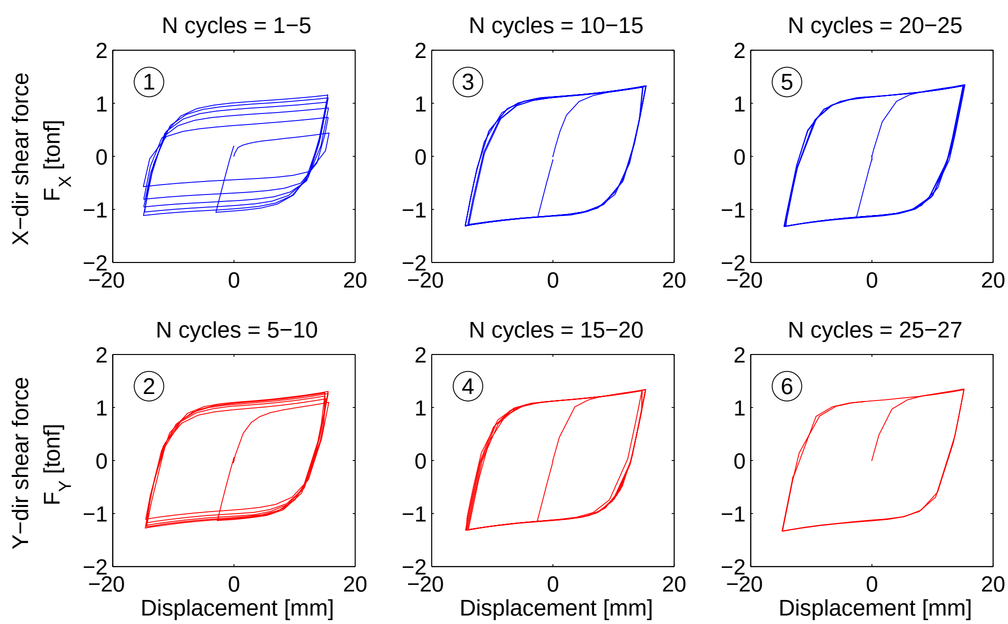

FIGURE 5.8. Force-deformation cycles of bi-directional numeric results of Cu-BEDD with geometry B.

The experimental results obtained for the unidirectional tests performed using devices with both geometries, A and B, prove the excellent behavior of the Cu-BEDD when subjected to cyclic deformation loading. In both cases, stable cycles with large energy dissipation capacity were obtained. In both devices plastic flow started at a relative displacement less than 0.5 mm, which indicates that the designed Cu-BEDDs work good as devices for small displacement demands. The devices were also capable of sustaining more than 20 cycles, and therefore, capable of enduring more than one strong earthquake. In the case of the bi-directional displacement test, the device exhibits the same desirable properties as in the unidirectional loading case: stable cycles, large energy dissipated, and large low-cycle fatigue life. In an actual structure, an array with several Cu-BEDD can be installed in order to obtain higher forces, according to the design requirements. If a new design for a larger deformation demand is needed, it can be obtained following the same design process used in this investigation.

6. CONCLUDING REMARKS

A copper-based energy dissipation device that works in two directions of displacement (Cu-BEDD) was successfully designed and tested, proving to have grate energy dissipation capacity and being capable of enduring more than one strong earthquake prior to failure. Copper was used as the base metal of the Cu-BEDD, due to the fact that it is a very plastic metal, it has a great performance when subjected to reversed cyclic loading, it can be smelted and reused once it has been damaged, and has outstanding corrosion-resistant qualities. Its cyclic behavior was modeled using a complete constitutive model developed by Chaboche, including kinematic and isotropic hardening, and the strain range effect, which are properties that influence the behavior of the Cu-BEDD under cyclic imposed relative displacements. The identification of the constitutive model parameters for ETP copper was successfully achieved using uniaxial strain-controlled tension-compresion tests by a process that can be replicated for any other metal that needs to be mathematically described by the Chaboche model. Using this constitutive model and a large deformations definition, a finite element model of the Cu-BEDD was developed proving to be very accurate in the prediction of the energy dissipated by the device, the force capacity, the cyclic hardening, the internal strain state, and the force-displacement response curves, with an average error of less than a $5\ \%$. The FE model was posteriorly used for the design of the Cu-BEDD geometry performed using the Response Surface Methodology. The method proved to be very cost-effective for the design process due to the fact that excessive experimental tests are avoided, and only the final design needs to be tested to validate the numerical design process.

In the design process of the Cu-BEDD, two main targets were pursued: (i) to obtain a response of the device to cyclic displacements with stable and large energy dissipating force-deformation cycles, at the minimal cost possible; and (ii) obtain a deign of a device capable of enduring the number of deformation cycles of at least one strong earthquake. In the case of the designed Cu-BEDD, both requirements were entirely fulfilled under both uni-directional and bi-directional cyclic deformation loading. An experimental testing campaign was performed using two Cu-BEDD prototypes designed for different displacement demands. The response of the tested devices under cyclic deformation loading, exhibit stable cycles with great energy dissipation capacity and low-cycle fatigue life. In every tested Cu-BEDD, plastic flow started at a relative displacement less than 0.5 mm, which makes the Cu-BEDD a very good candidate for an energy dissipation system in stiff structures where large relative displacement are scarce. Each device fracture was originated in the zone of maximum equivalent strain, and endured more than 20 cycles under maximum displacement amplitude, which according to the American Standards for the design of an energy dissipation device, corresponds more than one strong earthquake. One of the Cu-BEDD designed for 15 mm of relative displacement, was tested under a bi-directional cyclic displacement. The response obtained from the bi-directional test show stable cycles with large energy dissipation capacity and fatigue life, similar to the ones obtained from the uni-directional tests, therefore it can be concluded that the device works properly under both a bi-directional loading as well as a uni-directional loading. The devices are very versatile, they occupy a small volume in a structure and can be easily installed. Another interesting property is that if the force capacity required in the design of a seismic protection system of a structure is larger, several Cu-BEDD can be installed to work in parallel, so the maximum force increases proportional to the number of devices installed. Otherwise if larger displacements on the devices are required, the design process can be repeated for a larger displacement demand following the same steps shown in the present research. The design method is very versatile, it can be used for the design of other metal dampers using other metals, and it requires a minimal number of experimental tests of the device, since it uses the information obtained from cyclic axial tests of the base metal it is made of.

Further research can be done investigating the behavior the Cu-BEDD when installed in an actual structure, located in a position such that a two-dimensional relative displacement is demanded, as the case of a connection between two buildings, and the isolation systems with energy dissipating devices placed in a parallel set up. Other kind of metal dampers made of copper, such as the shear panel, the bucking restrained brace, the slit damper, and the honeycomb, can be investigated as well using the same method proposed in the present research. Also alternative metals to copper, such as aluminum, carbon steel, stainless steel, and copper-based alloys, can be used to design metallic dampers using this method, and obtain valuable information for a future product development.

References

Ansys Inc. (2009). *Ansys 12.1 user's manual*. Canonsburg, Pa, United States.

ASM Metals Handbook, Vol. 2. (2004). American Society of Metals.

Asm metals handbook, vol. 9. (2004). American Society of Metals.

Berbenni, S., Favier, V., & Berveiller, M. (2007, January). Impact of the grain size distribution on the yield stress of heterogeneous materials. *International Journal of Plasticity*, *23*(1), 114–142.

Black, C. J., Makris, N., & Aiken, I. D. (2004). Component Testing , Seismic Evaluation and Characterization of Buckling-Restrained Braces. *Journal of Structural Engineering*(June), 880–894.

Broggiato, G., Campana, F., & Cortese, L. (2008). The Chaboche nonlinear kinematic hardening model : calibration methodology and validation. *Meccanica*, *43*(2), 115–124.

Casciati, F., Faravelli, L., & Petrini, L. (1998). Energy Dissipation in Shape Memory Alloy Devices. *Computer-Aided Civil and Infrastructure Engineering*, *13*, 433–442.

Castellano, M. G., Colato, G. P., & Infanti, S. (2009). The experience of FIP Industriale in the retrofit of bridges trough seismic isolation and energy dissipation. *Buletinul AGIR*, *1*, 266–278.

Chaboche, J. L. (1986). Time-independent constitutive theories for cyclic plasticity. *International Journal of Plasticity*, *2*(2), 149–188.

Chaboche, J. L. (2008). A review of some plasticity and viscoplasticity constitutive theories. *Continuum*, *24*, 1642–1693.

Chan, R. W. K., & Albermani, F. (2008, April). Experimental study of steel slit damper for passive energy dissipation. *Engineering Structures*, *30*(4), 1058–1066.

Chiarotto, D., Tomaselli, F., Baldo, P., Castellano, M. G., & Infanti, S. (2004). Seismic protection of Tuy Medio Railway Viaducts: design and shaking table tests of the seismic devices. In *13th world conference on earthquake engineering vancouver, b.c., canada.*

Chou, C.-C., & Tsai, K.-C. (2002). Plasticity-fibre model for steel triangular plate energy dissipating devices. *Earthquake Engineering & Structural Dynamics*, *31*(9), 1643–1655.

Code Aster. (2008). *Code aster. version 11*. EDF, France.

Conrad, H. (2004). Grain-Size Dependence of the Flow Stress of Cu from Millimeters to Nanometers. *Metallurgical and Material Transactions A*, *35*(9), 2681–2695.

De la Llera, J. C., Esguerra, C., & Almazán, J. L. (2004, March). Earthquake behavior of structures with copper energy dissipators. *Earthquake Engineering & Structural Dynamics*, *33*(3), 329–358.

De Matteis, G., Landolfo, R., & Mazzolani, F. M. (2003, January). Seismic response of mr steel frames with low-yield steel shear panels. *Engineering Structures*, *25*(2), 155–168.

De Matteis, G., Mazzolani, F. M., & Panico, S. (2008, June). Experimental tests on pure aluminium shear panels with welded stiffeners. *Engineering Structures*, *30*(6), 1734–1744.

Franco, J. M., Cahís, X., Gracia, L., & López, F. (2010, September). Experimental testing of a new anti-seismic dissipator energy device based on the plasticity of metals. *Engineering Structures*, *32*(9), 2672–2682.

Jiang, Y. (2000). A fatigue criterion for general multiaxial loading. *Fatigue & Fracture of Engineering Materials & Structures*, *23*, 19–32.

Jiang, Y., & Zhang, J. (2008, September). Benchmark experiments and characteristic cyclic plasticity deformation. *International Journal of Plasticity*, *24*(9), 1481–1515.

Kim, J., & Choi, H. (2004, May). Behavior and design of structures with buckling-restrained braces. *Engineering Structures*, *26*(6), 693–706.

Kobori, T., Miura, Y., Fukuzawa, E., Yamada, T., Arita, T., Takenaka, Y., et al. (1992). Development and application of hysteresis steel dampers. In *Tenth world conference on earthquake engineering* (pp. 2341–2346).

Kobori, T., Yamada, T., Takenaka, Y., Maeda, Y., & Nishimura, I. (1988). Effect of dynamic tuned connector on reduction of seismic response -application to adjacent office buildings-. In *Proceedings of ninth world conference on earthquake engineering* (pp. 773–778 (V)).

Lee, M.-G., Kim, D., Kim, C., Wenner, M. L., Wagoner, R. H., & Chung, K. (2005). Spring-back evaluation of automotive sheets based on isotropic-kinematic hardening laws and non-quadratic anisotropic yield functions Part II : characterization of material properties. *International Journal of Plasticity*, *21*, 883–914.

Lemaitre, J., & Chaboche, J. L. (2000). *Mechanic of solid materials*. Cambridge University Press.

Li, J., Zhang, Z., Sun, Q., & Li, C. (2011, April). Low-cycle fatigue life prediction of various metallic materials under multiaxial loading. *Fatigue & Fracture of Engineering Materials & Structures*, *34*(4), 280–290.

López-Almansa, F., Castro-Medina, J. C., & Oller, S. (2012, August). A numerical model of the structural behavior of buckling-restrained braces. *Engineering Structures*, *41*, 108–117.

Luoh, T., & Chang, C. P. (1998). Effect of grain size / texture on the cyclic stress-strain behavior of polycrystalline copper. *Materials Science and Engineering A*, *256*, 18 – 24.

Manson, S. S. (1965). Fatigue: A complex subject-Some simple approximations. *Experimental Mechanics*, *5*(4), 193–226.

Martelli, A. (2008). Recent progress of applications of modern anti-seismic systems in europe-part 2 : Energy dissipation systems, shape memory alloy devices and shock transmitters. In *The 14th world conference on earthequake engineering, october 12-17, 2008, beijing, china.*

Matlab. (2010). *Matlab. version 7.10.0 (r2010a).* Natick, Massachusetts: The MathWorks Inc.

McCormick, J., & DesRoches, R. (2004). Damping Properties of Shape Memory Alloys for Seismic Applications. In *Proceedings of the 2004 structures congress* (pp. 1–11).

Miller, D. J., Fahnestock, L. A., & Eatherton, M. R. (2011). Self-Centering Buckling-Restrained Braces for Advanced Seismic Performance. In *Structures congress 2011 asce 2011 960* (pp. 960–970).

Moosbrugger, J. C., Morrison, D. J., & Jia, Y. (2000). Nonlinear kinematic hardening rule parameters - relationship to substructure evolution in polycrystalline nickel. *International Journal of Plasticity*, *16*(34), 439–467.

Moroni, M. O., Herrera, R., & Sarrazin, M. (2008). Testing of cu-based sma seismic energy dissipation devices. In *14 th world conference on earthquake engineering: Innovation practice safety.* International Association for Earthquake Engineering.

Nakashima, M., Iwai, S., Iwata, M., Takeuchi, T., Konomi, S., Akazawa, T., et al. (1994). Energy dissipation behaviour of shear panels made of low yield steel. *Earthquake Engineering & Structural Dynamics*, *23*(12), 1299–1313.

Pukelsheim, F. (2006). *Optimal Design of Experiments*. Society for Industrial and Applied Mathematics.

Rai, D. C., Annam, P. K., & Pradhan, T. (2013, January). Seismic testing of steel braced frames with aluminum shear yielding dampers. *Engineering Structures*, *46*, 737–747.

Rodgers, G. W., Denmead, C., Leach, N., & Chase, J. G. (2006). Experimental development and analysis of a high force/volume extrusion damper. In *New zealand society of earthquake engineering 2006 conference (nzsee 2006)* (Vol. c, p. 42).

Rodgers, G. W., Mander, J. B., Chase, J. G., Dhakal, R. P., Leach, N. C., & Denmead, C. S. (2008). Spectral analysis and design approach for high force-to-volume extrusion damper-based structural energy dissipation. (September 2007), 207–223.

Sahoo, D. R., & Rai, D. C. (2010, November). Seismic strengthening of non-ductile reinforced concrete frames using aluminum shear links as energy-dissipation devices. *Engineering Structures*, *32*(11), 3548–3557.

SEI/ASCE 7-05. (2006). *Minimum Design Loads for Buildings and Other Structures*. ASCE Publications.

Shen, K. L., & Soong, T. T. (1996, January). Design of Energy Dissipation Devices Based on Concept of Damage Control. *Journal of Structural Engineering*, *122*(1), 76–82.

SIRVE S.A. (2003). *Sirve, seismic protection technologies*.

Song, G., Ma, N., & Li, H.-N. (2006, July). Applications of shape memory alloys in civil structures. *Engineering Structures*, *28*(9), 1266–1274.

Soong, T. T., & Spencer Jr, B. F. (2002, March). Supplemental energy dissipation: state-of-the-art and state-of-the-practice. *Engineering Structures*, *24*(3), 243–259.

Stephens, R. I., Fatemi, A., Stephens, R. R., & Fuchs, H. O. (2001). *Metal Fatigue in Engineering*. Jhon Wiley & Son, Inc.

Symans, M. D., Charney, F. A., Whittaker, A. S., Constantinou, M. C., Kircher, C. A., Johnson, M. W., et al. (2008). Energy Dissipation Systems for Seismic Applications : Current Practice and Recent Developments. *Journal of Structural Engineering*, *134*(1), 3–21.

Tehranizadeh, M. (2001, June). Passive energy dissipation device for typical steel frame building in Iran. *Engineering Structures*, *23*(6), 643–655.

Tsai, K.-C., Chen, H.-W., Hong, C.-P., & Su, Y.-F. (1993). Design of Steel Triangular Plate Energy Absorbers for Seismic-Resistant Construction. *Earthquake Spectra*, *9*(3), 505–28.

Ucak, A., & Tsopelas, P. (2011). Constitutive Model for Cyclic Response of Structural Steels with Yield Plateau. *Journal of Structural Engineering*, *137*(2), 195–206.

Wang, C.-L., Usami, T., Funayama, J., & Imase, F. (2013, January). Low-cycle fatigue testing of extruded aluminium alloy buckling-restrained braces. *Engineering Structures*, *46*, 294–301.

Whittaker, A. S., Bertero, V. V., Thompson, C. L., & Alonso, L. J. (1991). Seismic Testing of Steel Plate Energy Dissipation Devices. *Earthquake Spectra*, *7*(4), 563–604.

Xia, C., & Hanson, R. D. (1992). Influence of ADAS Element Paramaters on Builidng Seismic Response. *Journal of Structural Engineering*, *118*(7), 1903–1918.

Zang, S. L., Guo, C., Thuillier, S., & Lee, M. G. (2011, June). A model of one-surface cyclic plasticity and its application to springback prediction. *International Journal of Mechanical Sciences*, *53*(6), 425–435.

Zhang, J., & Jiang, Y. (2005, November). An experimental investigation on cyclic plastic deformation and substructures of polycrystalline copper. *International Journal of Plasticity*, *21*(11), 2191–2211.

Zhang, J., & Jiang, Y. (2006, March). Fatigue of polycrystalline copper with different grain sizes and texture. *International Journal of Plasticity*, *22*(3), 536–556.